THE JOURNAL OF PHYSICAL CHEMISTRY C
A JOURNAL OF THE AMERICAN CHEMICAL SOCIETY

pubs.acs.org/JPCC

Article

Edge versus Interior Mn^{2+} Doping in 2D Layered Butylammonium Lead Bromide Perovskite Single Crystals

Taniya Dutta, Somnath M. Kashid, Rahul Hooda, Tariq Sheikh, Arindam Chowdhury, and Angshuman Nag*

Cite This: *J. Phys. Chem. C* 2022, 126, 21109−21116

Read Online

ACCESS | Metrics & More | Article Recommendations | Supporting Information

ABSTRACT: Butylammonium lead bromide [$(BA)_2PbBr_4$] has an atomically thin two-dimensional (2D) quantum well structure. So if Mn^{2+} ions are doped into such crystals, then one would expect efficient energy transfer from the strongly confined excitons to the dopants. Perhaps, the energy transfer happens to yield Mn^{2+} emission with a peak at 2.05 eV (605 nm). But significant excitonic emission is also observed, suggesting that the energy transfer process is not that efficient. Is there a spatial separation between Mn^{2+} ions and excitons reducing the energy transfer efficiency? To address this question, here, we study single crystals of Mn^{2+}-doped $(BA)_2PbBr_4$. The excitons located in the edge and interior of layers of $(BA)_2PbBr_4$ show different excitonic emissions. This difference allows us to separately probe the interaction of edge excitons and interior excitons with the Mn^{2+} ions, using temperature-dependent (7−300 K) photoluminescence (PL) spectroscopy and spatially resolved PL. We find that the edge excitons mainly sensitize the Mn^{2+} ions because Mn^{2+} doping is preferred near the layer edges. Both the poor doping concentration (0.6% Mn^{2+}) and edge doping lead to a large spatial separation between the interior excitons and dopant centers, reducing the energy transfer efficiency. These new insights will be helpful for the better design and application of luminescent Mn^{2+}-doped 2D layered hybrid perovskites.

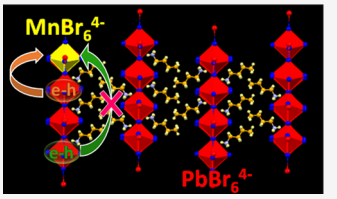

INTRODUCTION

Incorporation of Mn^{2+} as dopants into the lattice of quantum-confined semiconductors like ZnSe, CdSe, and $CsPbX_3$ (X = Cl, Br) nanocrystals leads to interesting optical, optoelectronic, and magneto-optic properties.[1−11] Energy transfer from the host exciton to the dopant, leading to Mn^{2+} d-electron emission, is one of the most studied properties in such samples. The increased overlap of the host exciton (or charge carriers) and the dopant in quantum-confined semiconductors significantly enhances the energy/charge transfer efficiency.[12,13] Therefore, it is natural to dope Mn^{2+} in two-dimensional (2D) layered organic−inorganic hybrid lead halide perovskites like butylammonium lead bromide [$(BA)_2PbBr_4$], with a quantum well structure.[14−16] The excitons are confined within the atomically thin Pb−Br inorganic layers. Consequently, one would expect a very efficient energy transfer from the host excitons to the dopants in Mn^{2+}-doped $(BA)_2PbBr_4$. But photoluminescence (PL) shows peaks originated from both the host excitons and the Mn^{2+} ions, suggesting an inefficient energy transfer process. Why so?

To address this question, we look into the relationship between the host's structure and the dopant's local structure. A single hybrid layer in $(BA)_2PbBr_4$ is shown in Figure 1a. Such layers stack together (Figure 1b) through van der Waals interactions forming the extended layered crystal.[17−21] In a typical Pb−Br inorganic layer, Mn^{2+} dopants can have two sites, namely, edge and interior, as denoted by red- and yellow-colored spheres, respectively, in Figure 1a. In the extended van der Waals solid, each of such inorganic layers provides the edge (red) and interior (yellow) doping sites for Mn^{2+} ions (see Figure 1b). It is expected to have breakages in the layers. Therefore, edge-doping sites are available deep inside the crystal as well. If Mn^{2+} ions are preferentially doped in the edge sites, then it might increase the spatial separation between the host excitons and dopant ions, reducing the energy transfer efficiency.

To elucidate the nature of doping, i.e., edge versus interior site doping, and the corresponding exciton−dopant interactions, we prepared single crystals of Mn^{2+}-doped $(BA)_2PbBr_4$[15] and studied temperature-dependent (7−300 K) PL spectroscopy and spatially resolved PL. Importantly, the PL of single crystals can distinguish between the interior and edge excitons,[22] as shown by e^-−h^+ pairs shown with yellow and red backgrounds, respectively, in Figure 1b. Therefore, single crystals are used here to distinguish the energy transfer processes from the interior and edge excitons to the dopant centers. Our results suggest that the dopant concentration is small (0.6%), along with preferential edge doping. Consequently, edge excitons predominantly sensitize the Mn^{2+}

Received: September 28, 2022
Revised: November 16, 2022
Published: December 1, 2022

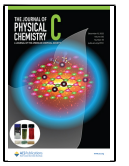

https://doi.org/10.1021/acs.jpcc.2c06911
J. Phys. Chem. C 2022, 126, 21109−21116

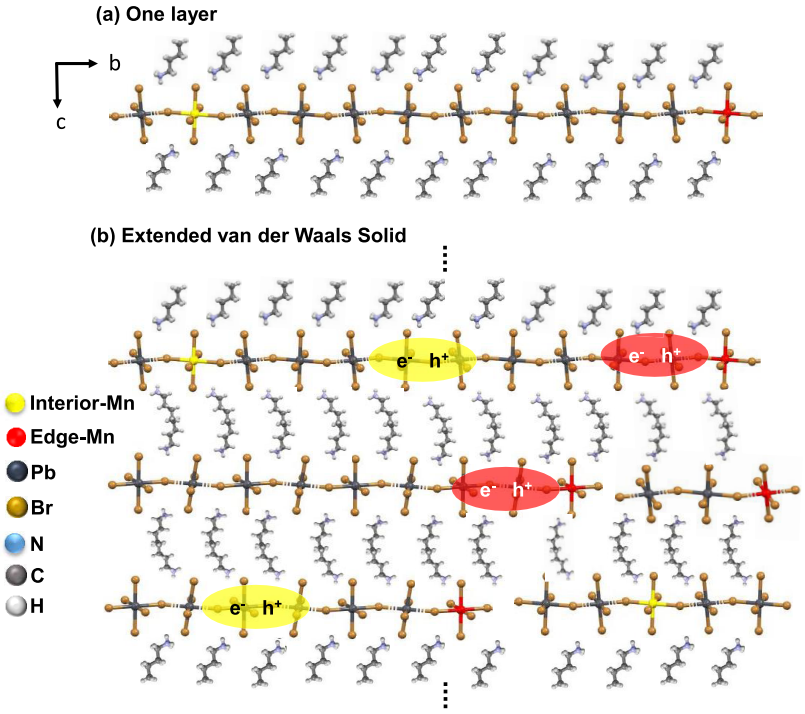

Figure 1. Schematic representation of the 2D layered hybrid perovskite structure of Mn^{2+}-doped $(BA)_2PbBr_4$. (a) One hybrid layer where the inorganic layer has two kinds of doping sites, edge and interior sites denoted by red- and yellow-colored spheres, respectively. (b) Infinite numbers (for simplicity, only three layers are shown here) of hybrid layers stack/assemble, forming an extended van der Waals solid. Each layer of the extended solid has both edge and interior sites. Some of the layers are expected to be broken, generating the edge sites deep inside the crystal as well. The excitons (e^-–h^+ pair) located near the interior and edge sites are presented by yellow and red backgrounds, respectively.

ions, leading to Mn^{2+} d-electron emission with a peak at 2.05 eV (605 nm). The interior excitons, though highly quantum-confined, are spatially separated from Mn^{2+} ions, leading to inefficient energy transfer. Furthermore, low-temperature PL shows that energy transfer is a thermally activated process.

METHODS

Synthesis of Butylammonium Bromide. Butylammonium bromide solution was prepared by mixing 468 μL of butylamine with 3 mL of hydrobromic acid (48% w/w aqueous) in an ice bath after minor modifications of the reported method.[15]

Synthesis of Mn^{2+}-Doped $(BA)_2PbBr_4$ Single Crystals. Both the doped and undoped samples were prepared after minor modifications of the reported[15] acid precipitation method. The only difference between the synthesis of undoped and doped samples is the addition of Mn^{2+} precursor in the synthesis of the doped sample. For a typical synthesis of Mn^{2+}-doped $(BA)_2PbBr_4$, PbO (558 mg, 2.5 mmol) and $MnBr_2$ (2147.48 mg, 10 mmol) were added in 3.5 mL of 48% w/w aqueous hydrobromic acid. The mixture was then heated at 80 °C to obtain a clear solution. Thereafter, a solution of 5 mmol of butylammonium bromide in 2.5 mL of 48% hydrobromic acid (48% w/w aqueous) was added to the above solution and heated at 100 °C for 10 min. The reaction temperature was then slowly (~10 °C/h) decreased to room temperature to grow flake-like single crystals with lateral sizes of about 6 mm and thicknesses of around 0.2 mm.

Characterization. Single-crystal X-ray diffraction (XRD) data were recorded using a Bruker Smart Apex Duo diffractometer equipped with Mo Kα radiation (λ = 0.71073 Å). The Bruker saint software package was used for integration by the narrow frame algorithm. Powder XRD data were recorded using a Bruker D8 Advance X-ray diffractometer equipped with Cu Kα radiation (1.54 Å). Field emission scanning electron microscopy (FESEM) measurements were done using a Zeiss Ultra Plus FESEM instrument. Inductively coupled plasma–optical emission spectroscopy (ICP-OES) measurements were performed using an ARCOS M/s apparatus (Spectro, Germany).

Optical Properties. All of the spectra were recorded from single crystals. A Shimadzu UV-3600 Plus UV–vis–NIR spectrophotometer was used to measure UV–visible diffuse reflectance spectra. The reflectance data were then converted to absorbance spectra following the Kubelka–Munk transformation.[23] Steady-state PL spectra and time-resolved PL decays were measured using an FLS 980 spectrometer (Edinburgh Instruments). To measure PL decays for excitonic emissions, 340 and 405 nm lasers were used as the excitation source, whereas, the decay of Mn^{2+} PL was measured after excitation with a microsecond flash lamp. The PL decay for exciton and Mn^{2+} emissions was fitted by biexponential and monoexponential decay equations, respectively. For biexponential decay, the average lifetimes were calculated by $\tau_{av} = \frac{\sum A_i \tau_i^2}{\sum A_i \tau_i}$, where A_i is the weighted average of lifetime τ_i. Low-temperature PL data were collected using the same setup (FLS 980, Edinburgh Instruments), after connecting it with a closed-cycle He-cryostat (Advanced Research Systems) and a Lakeshore temperature controller. Single crystals were glued on sapphire with a silver paste and mounted on the gold-coated sample holder.

Spatially Resolved PL Microscopy and Spectroscopy. PL imaging and spatially resolved spectroscopic measurements

https://doi.org/10.1021/acs.jpcc.2c06911
J. Phys. Chem. C 2022, 126, 21109–21116

were carried out using a home-built spectrally resolved laser epifluorescence microscopic setup, details of which can be found elsewhere.[24] In brief, the crystals were placed on a freshly cleaned coverslip and excited using a 405 nm laser (LaserGlow, LRD-0405PFR) via an oil immersive objective lens (Nikon TIRF 1.49NA 60× oil). The emission from samples was collected using the same objective lens, passed through appropriate dichroic and band-pass filters, and imaged using an sCMOS camera (Hamamatsu Orca flash4 V3). For spatially resolved PL spectroscopy, the emitted light was passed through a slit and a transmission grating (70 g/mm) placed before the sCMOS detector, which allowed us to obtain spectrally resolved images of a vertical strip along each crystal. All PL microscopy data were analyzed using ImageJ and Origin 7.5.

RESULTS AND DISCUSSION

Doping Efficacy, Structure, and Morphology. Mn^{2+}-doped $(BA)_2PbBr_4$ single crystals were synthesized by following the acid precipitation method reported earlier.[15] Elemental analysis by ICP-OES finds out that only 0.6% Mn^{2+} (with respect to Pb^{2+}) is present in the product, in spite of using a very high (400%) concentration of the Mn^{2+} precursor in the reaction mixture. The poor doping affinity of Mn^{2+} into the lattice of $(BA)_2PbBr_4$ might be attributed to the significantly smaller ionic size of Mn^{2+} (0.83 Å) in octahedral coordination compared to that of Pb^{2+} (1.19 Å).[25] Consequently, a large compressive strain develops upon Mn^{2+} doping. It is relatively easier for the edge sites to release such strain by structural reorganization; however, this process costs much more energy for the interior sites in this 2D crystal. The growth rate is slow for single crystals, and the lattice strain can be released by the ejection of the dopants toward the layer edges during the growth process. Therefore, relatively more doping density of Mn^{2+} is expected at the edge site of $(BA)_2PbBr_4$ compared to the interior sites. In general, doping might become more difficult in the single crystals of structurally low-dimensional hybrid perovskites.

Single-crystal XRD data for both undoped and doped samples were measured at 298 K. Refined structural parameters are shown in Table S1 of the Supporting Information (SI). The structures obtained from single-crystal XRD data of undoped and Mn^{2+}-doped samples are shown in Figures 2a and S1a, respectively. Both crystals possess an orthorhombic structure with the *Pbca* space group, similar to the earlier report[15] of undoped $(BA)_2PbBr_4$. Further, we find that the lattice parameters are nominally affected upon doping, consistent with the small (0.6%) Mn^{2+} doping obtained from ICP-OES data. The powder XRD patterns of both the undoped and doped samples are compared in Figure S2 in the SI. Both samples show similar (00*l*) planes in accordance with the periodic arrangement of hybrid layers in the crystal. The spacing between the two inorganic layers is estimated as 13.81 Å, which agrees with the single-crystal XRD data of $(BA)_2PbBr_4$. The FESEM images of undoped (Figure 2b) and doped (Figure S1b in the SI) samples show the layered morphology, which is attributed to their layered crystal structure.

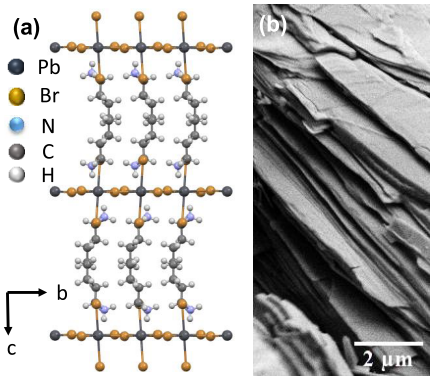

Figure 2. (a) Layered crystal structure of undoped $(BA)_2PbBr_4$ obtained from single-crystal XRD data. (b) FESEM image of a part of a $(BA)_2PbBr_4$ crystal showing the layered morphology.

Room-Temperature PL Probing Interaction of Edge and Interior Excitons with Mn^{2+} Dopants. The optical absorption and emission spectra of both samples are shown in Figures S3 and 3a, respectively. The undoped sample shows two absorption and emission features, which are attributed to excitonic transitions.[22,26] Based on the prior literature, we assign the lower energy emission peak at 2.84 eV (437 nm) to edge excitons, while the higher energy transition at 3.01 eV (412 nm) is designated to interior excitons. Following Mn^{2+} doping, the excitonic transition energies (spectral peak positions) do not change; however, a new emission peak appears at 2.05 eV (605 nm), which is attributed to the spin-forbidden $^4T_{1g} \rightarrow {}^6A_{1g}$ d−d transition of Mn^{2+} ions. We do not observe the corresponding feature in the absorption spectra, likely owing to the spin-forbidden nature of the d−d transition. Therefore, it is reasonable to conclude that the Mn^{2+} ions get excited to $^4T_{1g}$ via transferring the excitonic energy from the host,[14] and consequently, a lower energy-sensitized emission occurs from the dopant ions. We note that the subscript "g" is added in $^4T_{1g}$ and $^6A_{1g}$ because the Mn^{2+} ions have octahedral coordination in a centrosymmetric crystal (space group *Pbca*).

Subsequently, we collected PL excitation (PLE) spectra on the crystals to address whether both the edge and interior excitons have the same propensity to sensitize the Mn^{2+} dopants. The PLE spectra measured for the Mn^{2+} emission at 2.03 eV and for the edge exciton emission at 2.79 eV are found to be very similar (Figure 3b). This suggests that the excitation mechanism for both emissions is likely to be analogous, i.e., originate from the same source. The edge excitons are first created by light absorption, a proportion of which emit at 2.85 eV, while the remaining ones nonradiatively transfer excitation energy to the dopants, thereby leading to the characteristic Mn^{2+} emission with a peak at 2.05 eV. Importantly, the PLE spectra corresponding to the interior exciton emission (3.01 eV) are somewhat different from those of edge excitons and Mn^{2+} emission. For example, at 3.32 eV, both Mn^{2+} and edge exciton emissions have a broad feature; however, the interior exciton emission has a clear trough, as shown using a vertical line in Figure 3b. The PLE spectra suggest that although the major pathway of energy transfer to the Mn^{2+} dopant is from the edge excitons, some of the interior excitons can also transfer excitation energy to the Mn^{2+} dopants.

To better understand the modes of excitation energy transfer from the host to Mn^{2+} ions, time-resolved PL decay was recorded of both excitonic emissions for the doped as well as undoped samples. It is evident from the PL decay data (Figure 3c,d) that both excitonic emissions decay faster following Mn^{2+} doping. Interestingly, compared to interior exciton emission (Figure 3d), doping impacts the radiative decay of edge

https://doi.org/10.1021/acs.jpcc.2c06911
J. Phys. Chem. C 2022, 126, 21109−21116

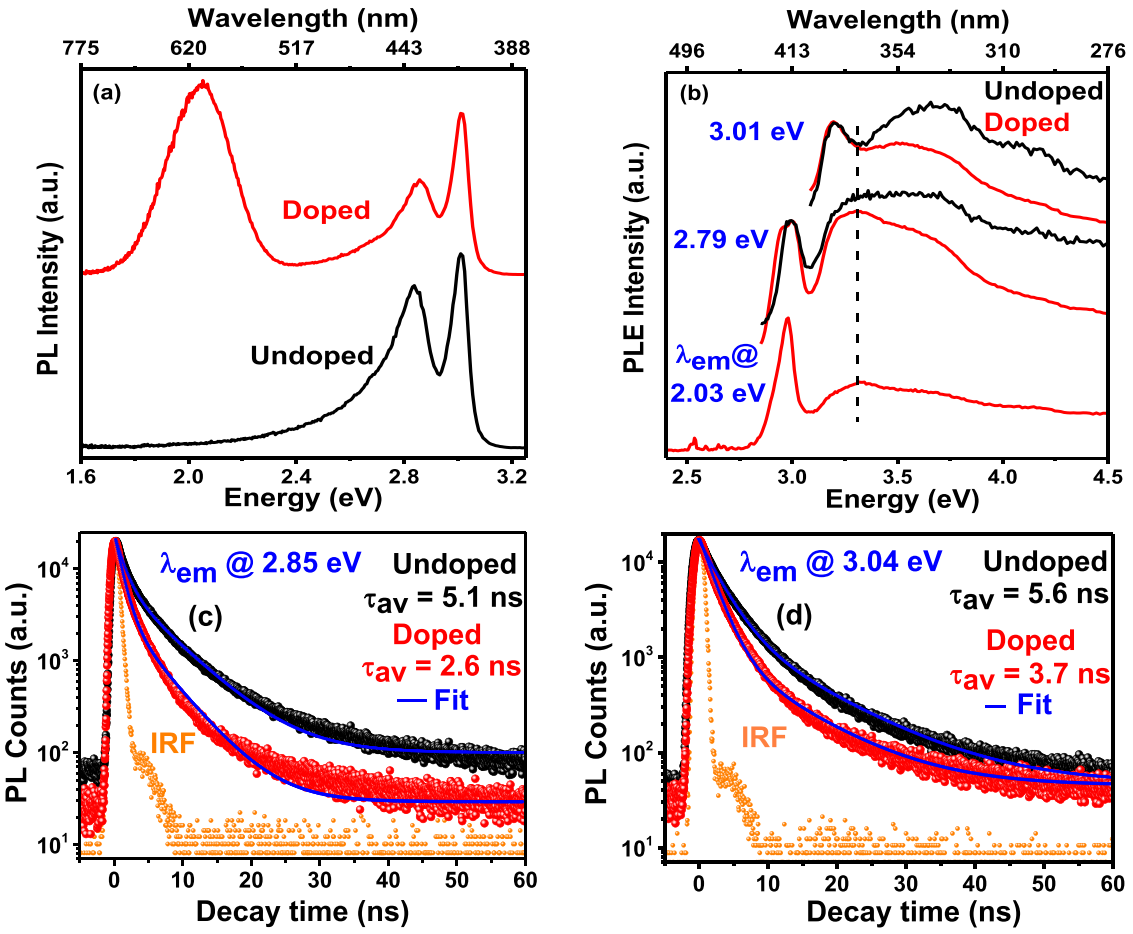

Figure 3. (a) Photoluminescence (PL) data of undoped and Mn^{2+}-doped $(BA)_2PbBr_4$ single crystals. (b) PL excitation (PLE) spectra of undoped and Mn^{2+}-doped $(BA)_2PbBr_4$ single crystals at three different emission energies corresponding to interior exciton (3.01 eV), edge exciton (2.79 eV), and Mn^{2+} (2.03 eV) emissions. PL and PLE intensities in (a) and (b) are shifted vertically for a clear presentation. Time-resolved PL decay of (c) edge exciton and (d) interior exciton for undoped and Mn^{2+}-doped $(BA)_2PbBr_4$ single crystals. IRF refers to instrument response function.

exciton emission more severely (Figure 3c). The biexponential fits to the PL decay profiles reveal that for the undoped sample, the edge excitons (at 2.85 eV) have an average lifetime of 5.1 ns (Figure 3c), with a fast component of 1.3 ns (70% contribution) and a slow component of 6.0 ns (30%). Identical analyses on the Mn^{2+}-doped samples show that the average lifetime of the edge excitons drastically reduces to 2.7 ns with faster and slower lifetimes of 1.1 ns (86%) and 4.8 ns (14%), respectively. The faster lifetime typically has contributions from nonradiative decay processes. Our observation that the contribution of the faster lifetime increases significantly in the Mn^{2+}-doped samples is consistent with additional energy transfer pathways from the edge excitons to the Mn^{2+} ions.

We find that the interior excitons (λ_{em}@3.04 eV) in the undoped sample decay with an average PL lifetime of 5.6 ns (Figure 3d), with fast and slow lifetime components of 2.8 ns (86%) and 10.4 ns (14%), respectively. Further, the average lifetime for these excitons in the doped samples decrease slightly to 3.7 ns, with corresponding fast and slow components of 2.0 ns (93%) and 9.0 ns (7%), respectively. This decrease in PL lifetime after Mn^{2+} doping can be rationalized either by direct sensitization of Mn^{2+} dopants from interior excitons or via increased nonradiative energy transfer from the interior to edge excitons upon Mn^{2+} doping. Nonetheless, the overall decrease in the average PL lifetime of interior excitons upon Mn^{2+} doping is considerably less with respect to that for the edge excitons. This suggests the enhanced efficiency of excitation energy transfer from the edge excitons to Mn^{2+} dopants compared to that for the interior excitons.

Spatially Resolved PL Spectroscopy. To gain more insights, we employ spatially resolved PL imaging and spectroscopy using a home-built wide-field epifluorescence microscopy setup.[24] The PL image of a part of a single crystal of Mn^{2+}-doped $(BA)_2PbBr_4$ excited with a 405 nm (3.06 eV) laser is shown in Figure 4a. A clear heterogeneity in emission intensity at the edge and the interior regions of the crystal is observed. However, the emission from different locations of a single crystal needs to be spectrally resolved to interpret the origin of the observed heterogeneity. A large-sized layered crystal allows us to perform the spatially resolved spectroscopic measurements from multiple diffraction-limited nanodomains (~250 nm full width at half-maximum (FWHM)) at the edge and the interior regions of the crystal. Emission spectra at three different locations, two from the interior and one at the edge (marked as 1, 2, and 3 in Figure 4a) of the crystal, are shown in Figure 4b. The Mn^{2+} emission peak around 605 nm could be clearly observed in all three locations. Both the spectral shape and transition energy of Mn^{2+} emission remain similar for all dopant locations, indicating similar octahedral ligand field splitting for all of the Mn^{2+} dopants. This similarity of the $[MnBr_6]^{4-}$ octahedron in the interior and layer edge will also

https://doi.org/10.1021/acs.jpcc.2c06911
J. Phys. Chem. C 2022, 126, 21109−21116

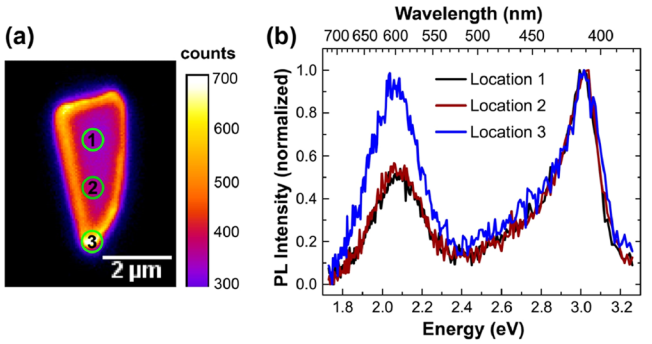

Figure 4. (a) Pseudocolor PL intensity image of a Mn^{2+}-doped $(BA)_2PbBr_4$ single crystal. (b) Spatially resolved PL emission spectra of regions 1, 2, and 3. Locations (1, 2, and 3) are marked in figure (a).

make it difficult to distinguish the two kinds of Mn^{2+} dopants using characterization techniques such as electron paramagnetic resonance spectroscopy.[15]

We note that the blue edge of the excitonic peak from the host is partially obscured owing to the scattering of the 405 nm laser excitation by the large crystal. The peak at 3.02 eV (410 nm) observed in Figure 4b has a large contribution from the scattered excitation light, which partially overlaps with excitonic emissions. We were able to minimize the scattering by using an emission filter and decreasing the laser excitation power, resulting in a minimal change in scattering intensity at different locations. To compare the relative intensity of Mn^{2+} emission at the edge and interior of the crystal, we normalized the emission spectra with the scattering peak intensity at 3.02 eV (410 nm). To ensure that such normalization does not affect the Mn^{2+} emission, PL spectroscopic measurements were performed on both Mn^{2+}-doped and undoped $(BA)_2PbBr_4$ single crystals, which revealed a similar scattering intensity ratio between the interior and edges for both (see Figure S4 in the SI). Interestingly, for more than 20 doped crystals investigated, we consistently find that the Mn^{2+} PL centered around 605 nm has more dominant emissivity at the edges compared to the interior regions. Thus, the spatially resolved PL spectra further support our inference that Mn^{2+} emission preferentially originates from layer/crystal edges of Mn^{2+}-doped $(BA)_2PbBr_4$ single crystals.

PLE (Figure 3b), PL decay (Figure 3c,d), and spatially resolved PL (Figure 4) data suggest that the Mn^{2+} emission originates preferentially from the Mn^{2+} dopants located near the layer edges. These findings, along with poor 0.6% doping (in spite of adding 400% Mn^{2+} precursor to the reaction mixture), indicate that the doping preferentially happens near the layer edges. The efficiency of the energy transfer process from the exciton to the dopant decreases sharply with increasing distance between them.[12] Therefore, the energy transfer efficiency from the interior exciton (yellow background of Figure 1b) to Mn^{2+} ions is lesser compared to the edge exciton (red background of Figure 1b). However, the presence of a smaller fraction of dopants in the interior cannot be ruled out, and efficient energy transfer is possible from interior excitons located near the interior dopant ions as well. Further, we note that the exciton diffusion length is quite large (~40 nm) for similar 2D layered perovskites.[27,28] So, there is a possibility of interior exciton diffusion through the layer to reach closer to Mn^{2+} ions near layer edges, leading to the energy transfer and subsequent Mn^{2+} emission. Overall, our results suggest that, in spite of the high quantum confinement of excitons (Bohr radius ~1 nm)[29] in such 2D layered hybrid perovskites, the exciton−dopant distance is large because of the small dopant concentration and inhomogeneous doping. Consequently, the energy transfer efficiency (particularly from interior excitons) is nominal, yielding significant exciton emissivity in the PL spectrum of Mn^{2+}-doped samples. We note here that recent reports suggest that doping lanthanide ions in such layered 2D perovskites is also very difficult along with inefficient host-to-dopant energy transfer.[30,31]

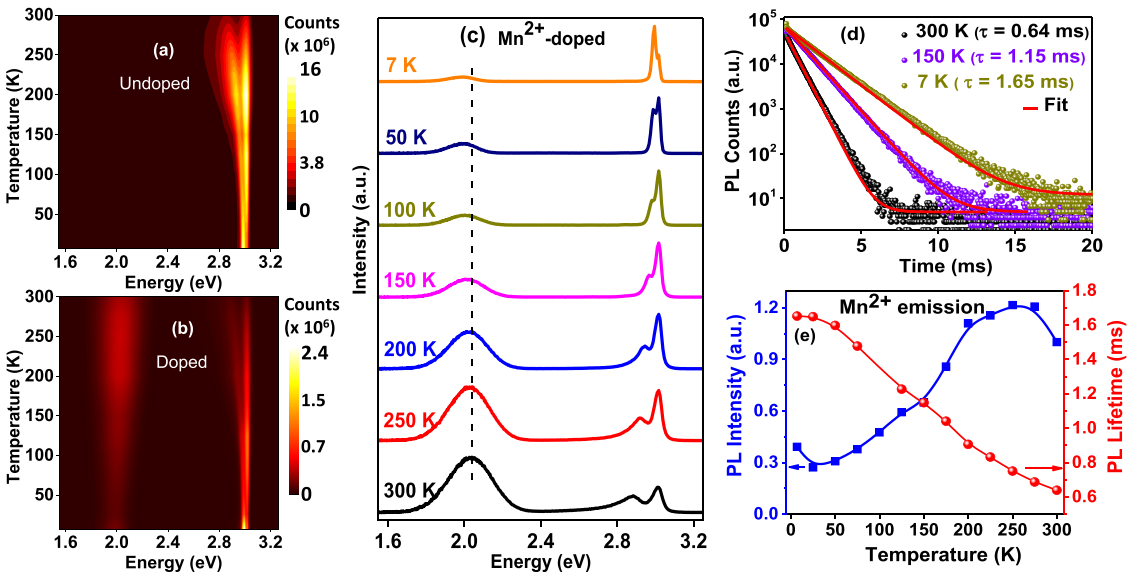

Figure 5. Pseudocolor emission intensity map of (a) undoped and (b) Mn^{2+}-doped $(BA)_2PbBr_4$ single crystals. Note that the PL intensity depends on the position and geometry of the sample when placed between the excitation source and the detector, and hence, the emissivity of the two samples cannot be compared directly. (c) Temperature-dependent PL spectra of Mn^{2+}-doped $(BA)_2PbBr_4$ single crystals. (d) PL decay dynamics of Mn^{2+}-doped $(BA)_2PbBr_4$ measured at different temperatures. (e) Temperature-dependent integrated PL intensity and lifetime of Mn^{2+} emission arising from Mn^{2+}-doped $(BA)_2PbBr_4$ single crystals.

https://doi.org/10.1021/acs.jpcc.2c06911
J. Phys. Chem. C 2022, 126, 21109−21116

Low-Temperature PL. To gain further insights into the energy transfer processes, we performed temperature-dependent PL measurements in the range of 7−300 K. The single-crystal XRD data of $(BA)_2PbBr_4$ measured at 100 K (see Table S2 in the SI) shows that the crystal structure remains unchanged compared to the data measured at room temperature (298 K). The temperature-dependent PL spectra of $(BA)_2PbBr_4$ shown in Figure S5 in the SI and the corresponding pseudocolor map shown in Figure 5a do not show any sudden change, indicating the absence of a temperature-dependent structural phase transition. Similar changes in the excitonic emission with temperature have been reported earlier for such 2D layered perovskites and are therefore not discussed here in detail.[32,33] Instead, we mainly focus on the excitation and emission processes of Mn^{2+} d-electrons in Mn^{2+}-doped $(BA)_2PbBr_4$. While there are a few recent reports of the low-temperature PL study of Mn^{2+}-doped in 2D layered perovskites down to 77 K,[16,34,35] there are no reports on PL spectral and PL lifetime measurements on such systems down to 7 K. More importantly, we emphasize that the Mn^{2+} dopants near the layer edges predominantly contribute to the observed Mn^{2+} emission, and therefore, we probe the temperature dependence of Mn^{2+} emission arising from such edge-dopant sites.

Mn^{2+}-doped $(BA)_2PbBr_4$ shows the additional Mn^{2+} emission peak around 2.0 eV in the entire temperature range (7−300 K), as evident from the pseudocolor map shown in Figure 5b. The corresponding PL spectra at a few representative temperatures between 7 and 300 K are shown in Figure 5c. We find that the Mn^{2+} emission peak systematically red-shifts with decreasing temperature (2.05 eV at 300 K to 1.99 eV at 7 K). The red shift of Mn^{2+} PL with decreasing temperature is consistent with the previous reports, which is attributed to an increase in crystal field splitting of the $^4T_{1g}$ state due to compression of the host lattice at lower temperatures and may also be a consequence of depopulation of the vibronic hot band.[36−38] Figure S6 in the SI reveals that the spectral width of the Mn^{2+} emission decreases with the lowering of temperature owing to the suppression of lattice vibrations.

Figures 5d and S7 show the lifetimes of Mn^{2+} emission at different temperatures, which are all quasi-single exponential in nature. At 300 K, the lifetime for Mn^{2+} emission is found to be 0.639 ms; such a long lifetime is attributed to the spin- and parity-forbidden $^4T_{1g} \rightarrow {}^6A_{1g}$ d−d transition of Mn^{2+} ions. Upon lowering the temperature, the PL lifetime systematically increases from ∼0.64 ms (at 300 K) to ∼1.65 ms at 7 K (Figure 5e). Such an increase in PL lifetimes likely owes to the suppression of nonradiative relaxation processes as the temperature is lowered, which should therefore be associated with an increase in emission intensity. While we do observe an increase in the emissivity from 300 to 250 K, intriguingly, upon further lowering of temperature, we find that Mn^{2+} emission intensity decreases continuously down to ∼25 K and then increases slightly at 7 K (Figure 5e). This unusual trend illustrated that the correlation of the dopant emission intensity with its lifetime is not straightforward, and perhaps, some other processes are operational within the range of 25−250 K. We note that the PL lifetime is solely governed by the relaxation process of the $^4T_{1g}$ state, while the emission intensity depends both on the excitation process populating the $^4T_{1g}$ state and on subsequent relaxation processes. Therefore, it is reasonable to infer that the decrease in emission intensity below 250 K owes to the suppression of the excitation process, which populates the $^4T_{1g}$ (Mn^{2+}) state.

The decrease in PL intensity below 250 K further suggests that the energy transfer from host excitons to Mn^{2+} dopant ions is a thermally activated process. Figure 6 schematically depicts the excitation and emission processes of Mn^{2+}-doped $(BA)_2PbBr_4$. The host absorbs the incident photons generating both interior and edge excitons. A subpopulation of those excitons radiatively recombine at slightly different energies, and the remaining ones transfer their energy to sensitize Mn^{2+} dopants, which eventually emit at 2.05 eV (605 nm). Our results depicted in Figures 3 and 4 suggest that the edge exciton is relatively more efficient in transferring the energy to Mn^{2+} ions compared to the interior excitons. Further, the low-temperature PL data (Figure 5) suggest that the energy transfer is a thermally activated process, as indicated by the energy barrier "Δ*E*" depicted in Figure 6. Prior reports suggest that the energy transfer process in Mn^{2+} II−VI semiconductor nanocrystals and Mn^{2+} doped in $CsPbX_3$ (X: Cl, Br) perovskite nanocrystals and bulk samples proceed via transient charge transfer states (CTS) like Mn^{3+} or shallow traps.[39−44] Such a situation might occur in our samples as well; however, at this stage, we do not have sufficient experimental evidence to conclusively comment on whether transient CTS and/or traps mediate the host-to-dopant energy transfer process. However, it is likely that the energy transfer process involves the excitation of higher energy levels of Mn^{2+} ions (such as $^4T_{2g}$), eventually yielding PL emission owing to the $^4T_{1g}$-to-$^6A_{1g}$ transition.

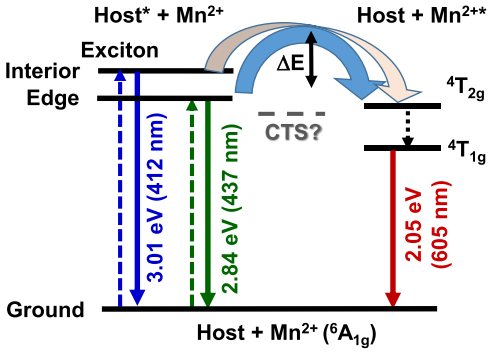

Figure 6. Schematics of excitation and emission processes in Mn^{2+}-doped $(BA)_2PbBr_4$ single crystals. The ground state represents the total energy of the host and Mn^{2+} in $^6A_{1g}$.[45] Excited states (host* + Mn^{2+}) represent the host with an exciton (either interior or edge) and Mn^{2+} in $^6A_{1g}$. Another set of excited states (host + Mn^{2+}*) represent the host along with Mn^{2+} in $^4T_{1g}$ or $^4T_{2g}$. Both the interior exciton (blue arrows) and edge excitons (green arrows) are responsible for light absorption (upward arrow) and emission (downward arrow). Energy transfer from edge excitons to Mn^{2+} ions is more efficient and therefore indicated by the thicker blue-colored curved arrow, whereas the lower efficacy of the energy transfer process from the interior exciton is shown by a thinner curved arrow. "Δ*E*" indicates the thermal activation energy required for the energy transfer. The exited state of Mn^{2+} ions then relaxes back to the ground state by emitting 2.05 eV light (red-colored downward arrow). The black-colored broken arrow indicates possible nonradiative relaxation processes from $^4T_{2g}$ to $^4T_{1g}$. Transient charge transfer states (CTSs) like Mn^{3+} (or other trap states) might mediate the energy transfer process.

https://doi.org/10.1021/acs.jpcc.2c06911
J. Phys. Chem. C 2022, 126, 21109−21116

CONCLUSIONS

We prepared single crystals of Mn^{2+}-doped $(BA)_2PbBr_4$ 2D layered hybrid perovskites. In spite of using 400% Mn^{2+} in the reaction mixture with respect to Pb^{2+} ions, doping is found to be difficult, yielding only 0.6% Mn^{2+} in the product. Single-crystal XRD data of the undoped and Mn^{2+}-doped samples are very similar without any noticeable change in the lattice parameters. The single crystals show two kinds of excitonic PL emissions with transitions at 2.84 and 3.01 eV, characteristic of edge excitons and interior excitons, respectively. PL excitation spectra, time-resolve PL decay, and spatially resolved PL spectral measurements reveal that the edge excitons more efficiently sensitize the Mn^{2+} dopants compared to the interior excitons, resulting in Mn^{2+} emission at 2.05 eV. Our results suggest that the doping in the interior of the 2D inorganic layers is rather challenging; instead, the Mn^{2+} ions are preferentially located near the layer edges. Owing to the lack of proximity between the interior exciton and Mn^{2+} ions, the efficacy of the host-to-dopant energy transfer process is low. Perhaps, smaller (~a few tens of nanometers) crystals of 2D hybrid perovskite can enhance the proximity between excitons and Mn^{2+} ions without altering the excitonic confinement (Bohr radius ~1 nm) and can thereby facilitate efficient energy transfer from hosts to dopants. Furthermore, the temperature (7−300 K)-dependent PL data show that the energy transfer is a thermally activated process and might involve shallow traps or charge transfer states. The insights provided here into Mn^{2+} doping in the interior versus edge sites of 2D hybrid perovskite and the corresponding host-to-dopant energy processes should aid the future development of this class of material as a functional luminescent and optoelectronic material.

ASSOCIATED CONTENT

Supporting Information

The Supporting Information is available free of charge at https://pubs.acs.org/doi/10.1021/acs.jpcc.2c06911.

Crystallographic data obtained from single-crystal XRD analysis; FESEM images; UV−visible absorption; statistics on spatially resolved PL data; low-temperature PL spectra; and low-temperature PL decay data (PDF)

BA2PbBr4_100K.cif (CIF)

BA2PbBr4_RT.cif (CIF)

Mn_(BA)2PbBr4_RT.cif (CIF)

Mn_BA2PbBr4_100K.cif (CIF)

AUTHOR INFORMATION

Corresponding Author

Angshuman Nag − *Department of Chemistry, Indian Institute of Science Education and Research (IISER) Pune, Pune 411008, India;* orcid.org/0000-0003-2308-334X; Email: angshuman@iiserpune.ac.in

Authors

Taniya Dutta − *Department of Chemistry, Indian Institute of Science Education and Research (IISER) Pune, Pune 411008, India*

Somnath M. Kashid − *Department of Chemistry, Indian Institute of Technology Bombay, Mumbai 400076, India*

Rahul Hooda − *Department of Chemistry, Indian Institute of Science Education and Research (IISER) Pune, Pune 411008, India*

Tariq Sheikh − *Department of Chemistry, Indian Institute of Science Education and Research (IISER) Pune, Pune 411008, India;* orcid.org/0000-0002-4863-9642

Arindam Chowdhury − *Department of Chemistry, Indian Institute of Technology Bombay, Mumbai 400076, India;* orcid.org/0000-0001-8178-1061

Complete contact information is available at: https://pubs.acs.org/10.1021/acs.jpcc.2c06911

Notes

The authors declare no competing financial interest.

ACKNOWLEDGMENTS

A.N. acknowledges the Science & Engineering Research Board (Swarnajayanti Fellowship, SB/SJF/2020-21/02) India. T.D. and T.S. acknowledge University Grants Commission (UGC) India for research fellowships. A.C. acknowledges SERB (India, Grant No. EMR/2017/004878) for financial support. S.M.K. thanks IIT Bombay for the institute postdoctoral fellowship.

REFERENCES

(1) Norris, D. J.; Yao, N.; Charnock, F. T.; Kennedy, T. A. High-Quality Manganese-Doped ZnSe Nanocrystals. *Nano Lett.* **2001**, *1*, 3−7.

(2) Beaulac, R.; Archer, P. I.; van Rijssel, J.; Meijerink, A.; Gamelin, D. R. Exciton Storage by Mn^{2+} in Colloidal Mn^{2+}-Doped CdSe Quantum Dots. *Nano Lett.* **2008**, *8*, 2949−2953.

(3) Santra, P. K.; Kamat, P. V. Mn-Doped Quantum Dot Sensitized Solar Cells: A Strategy to Boost Efficiency over 5%. *J. Am. Chem. Soc.* **2012**, *134*, 2508−2511.

(4) Guria, A. K.; Dutta, S. K.; Adhikari, S. D.; Pradhan, N. Doping Mn^{2+} in Lead Halide Perovskite Nanocrystals: Successes and Challenges. *ACS Energy Lett.* **2017**, *2*, 1014−1021.

(5) Pradhan, N.; Das Adhikari, S.; Nag, A.; Sarma, D. D. Luminescence, Plasmonic, and Magnetic Properties of Doped Semiconductor Nanocrystals. *Angew. Chem., Int. Ed.* **2017**, *56*, 7038−7054.

(6) Mir, W. J.; Mahor, Y.; Lohar, A.; Jagadeeswararao, M.; Das, S.; Mahamuni, S.; Nag, A. Postsynthesis Doping of Mn and Yb into $CsPbX_3$ (X = Cl, Br, or I) Perovskite Nanocrystals for Down-conversion Emission. *Chem. Mater.* **2018**, *30*, 8170−8178.

(7) Mir, W. J.; Swarnkar, A.; Nag, A. Postsynthesis Mn-Doping in $CsPbI_3$ Nanocrystals to Stabilize the Black Perovskite Phase. *Nanoscale* **2019**, *11*, 4278−4286.

(8) Pradhan, N. Mn-Doped Semiconductor Nanocrystals: 25 Years and Beyond. *J. Phys. Chem. Lett.* **2019**, *10*, 2574−2577.

(9) Cao, F.; Yu, D.; Xu, X.; Cai, B.; Gu, Y.; Dong, Y.; Shen, Y.; Zeng, H. Water-Assisted Synthesis of Blue Chip Excitable 2D Halide Perovskite with Green-Red Dual Emissions for White LEDs. *Small Methods* **2019**, *3*, No. 1900365.

(10) Paul, S.; Bladt, E.; Richter, A. F.; Döblinger, M.; Tong, Y.; Huang, H.; Dey, A.; Bals, S.; Debnath, T.; Polavarapu, L.; Feldmann, J. Manganese-Doping-Induced Quantum Confinement within Host Perovskite Nanocrystals through Ruddlesden−Popper Defects. *Angew. Chem., Int. Ed.* **2020**, *59*, 6794−6799.

(11) Dey, A.; Ye, J.; De, A.; Debroye, E.; Ha, S. K.; Bladt, E.; Kshirsagar, A. S.; Wang, Z.; Yin, J.; Wang, Y.; et al. State of the Art and Prospects for Halide Perovskite Nanocrystals. *ACS Nano* **2021**, *15*, 10775−10981.

(12) Chen, H.-Y.; Maiti, S.; Son, D. H. Doping Location-Dependent Energy Transfer Dynamics in Mn-Doped CdS/ZnS Nanocrystals. *ACS Nano* **2012**, *6*, 583−591.

(13) Mir, W. J.; Jagadeeswararao, M.; Das, S.; Nag, A. Colloidal Mn-Doped Cesium Lead Halide Perovskite Nanoplatelets. *ACS Energy Lett.* **2017**, *2*, 537−543.

(14) Biswas, A.; Bakthavatsalam, R.; Kundu, J. Efficient Exciton to Dopant Energy Transfer in Mn^{2+}-Doped $(C_4H_9NH_3)_2PbBr_4$ Two-Dimensional (2D) Layered Perovskites. *Chem. Mater.* **2017**, *29*, 7816−7825.
(15) Sheikh, T.; Nag, A. Mn Doping in Centimeter-Sized Layered 2D Butylammonium Lead Bromide (BA_2PbBr_4) Single Crystals and Their Optical Properties. *J. Phys. Chem. C* **2019**, *123*, 9420−9427.
(16) Zhang, H.; Yao, J.; Zhou, K.; Yang, Y.; Fu, H. Thermally Activated Charge Transfer in Dual-Emission Mn^{2+}-Alloyed Perovskite Quantum Wells for Luminescent Thermometers. *Chem. Mater.* **2022**, *34*, 1854−1861.
(17) Sapori, D.; Kepenekian, M.; Pedesseau, L.; Katan, C.; Even, J. Quantum Confinement and Dielectric Profiles of Colloidal Nanoplatelets of Halide Inorganic and Hybrid Organic−Inorganic Perovskites. *Nanoscale* **2016**, *8*, 6369−6378.
(18) Stoumpos, C. C.; Cao, D. H.; Clark, D. J.; Young, J.; Rondinelli, J. M.; Jang, J. I.; Hupp, J. T.; Kanatzidis, M. G. Ruddlesden−Popper Hybrid Lead Iodide Perovskite 2D Homologous Semiconductors. *Chem. Mater.* **2016**, *28*, 2852−2867.
(19) Ghimire, S.; Klinke, C. Two-Dimensional Halide Perovskites: Synthesis, Optoelectronic Properties, Stability, and Applications. *Nanoscale* **2021**, *13*, 12394−12422.
(20) Laxmi; Kabra, D. Origin of Contrasting Emission Spectrum of Bromide versus Iodide Layered Perovskite Semiconductors. *J. Phys. Chem. Lett.* **2022**, *13*, 2737−2743.
(21) Steger, M.; Janke, S. M.; Sercel, P. C.; Larson, B. W.; Lu, H.; Qin, X.; Yu, V. W.-Z.; Blum, V.; Blackburn, J. L. On the Optical Anisotropy in 2D Metal-Halide Perovskites. *Nanoscale* **2022**, *14*, 752−765.
(22) Sheikh, T.; Nawale, V.; Pathoor, N.; Phadnis, C.; Chowdhury, A.; Nag, A. Molecular Intercalation and Electronic Two Dimensionality in Layered Hybrid Perovskites. *Angew. Chem., Int. Ed.* **2020**, *59*, 11653−11659.
(23) Kubelka, P.; Munk, F. An Article on Optics of Paint Layers. *Z. Tech. Phys.* **1931**, *12*, 593.
(24) Sharma, D. K.; Chowdhury, A. Spectrally Resolved Optical Microscopy Using a Transmission Grating Spectrograph: Importance of Spatial Selection. *Analyst* **2014**, *139*, 473−481.
(25) Shannon, R. D. Revised Effective Ionic Radii and Systematic Studies of Interatomic Distances in Halides and Chalcogenides. *Acta Crystallogr., Sect. A* **1976**, *32*, 751−767.
(26) Sheikh, T.; Shinde, A.; Mahamuni, S.; Nag, A. Possible Dual Bandgap in $(C_4H_9NH_3)_2PbI_4$ 2D Layered Perovskite: Single-Crystal and Exfoliated Few-Layer. *ACS Energy Lett.* **2018**, *3*, 2940−2946.
(27) Seitz, M.; Magdaleno, A. J.; Alcázar-Cano, N.; Meléndez, M.; Lubbers, T. J.; Walraven, S. W.; Pakdel, S.; Prada, E.; Delgado-Buscalioni, R.; Prins, F. Exciton Diffusion in Two-Dimensional Metal-Halide Perovskites. *Nat. Commun.* **2020**, *11*, No. 2035.
(28) Deng, S.; Shi, E.; Yuan, L.; Jin, L.; Dou, L.; Huang, L. Long-Range Exciton Transport and Slow Annihilation in Two-Dimensional Hybrid Perovskites. *Nat. Commun.* **2020**, *11*, No. 664.
(29) Tanaka, K.; Takahashi, T.; Kondo, T.; Umebayashi, T.; Asai, K.; Ema, K. Image Charge Effect on Two-Dimensional Excitons in an Inorganic-Organic Quantum-Well Crystal. *Phys. Rev. B* **2005**, *71*, No. 045312.
(30) Cortecchia, D.; Mróz, W.; Folpini, G.; Borzda, T.; Leoncino, L.; Alvarado-Leaños, A. L.; Speller, E. M.; Petrozza, A. Layered Perovskite Doping with Eu^{3+} and B-Diketonate Eu^{3+} Complex. *Chem. Mater.* **2021**, *33*, 2289−2297.
(31) Mondal, B.; Poovathan, A.; Sheikh, T.; Nag, A. Yb^{3+}-Doped Phenylethylammonium Lead Bromide 2D Layered Hybrid Perovskite for Near-Infrared Emission. *ChemNanoMat* **2022**, *8*, No. e202200104.
(32) Dutta, T.; Sheikh, T.; Nag, A. Temperature-Dependent Photoluminescence of Hexafluorobenzene-Intercalated Phenethylammonium Tin Iodide 2D Perovskite. *Chem.—Asian J.* **2021**, *16*, 2745−2751.
(33) Kahmann, S.; Duim, H.; Fang, H.-H.; Dyksik, M.; Adjokatse, S.; Rivera Medina, M.; Pitaro, M.; Plochocka, P.; Loi, M. A. Photophysics of Two-Dimensional Perovskites—Learning from Metal Halide Substitution. *Adv. Funct. Mater.* **2021**, *31*, No. 2103778.
(34) Bakthavatsalam, R.; Biswas, A.; Chakali, M.; Bangal, P. R.; Kore, B. P.; Kundu, J. Temperature-Dependent Photoluminescence and Energy-Transfer Dynamics in Mn^{2+}-Doped $(C_4H_9NH_3)_2PbBr_4$ Two-Dimensional (2D) Layered Perovskite. *J. Phys. Chem. C* **2019**, *123*, 4739−4748.
(35) Su, B.; Molokeev, M. S.; Xia, Z. Unveiling Mn^{2+} Dopant States in Two-Dimensional Halide Perovskite toward Highly Efficient Photoluminescence. *J. Phys. Chem. Lett.* **2020**, *11*, 2510−2517.
(36) Nag, A.; Cherian, R.; Mahadevan, P.; Gopal, A. V.; Hazarika, A.; Mohan, A.; Vengurlekar, A. S.; Sarma, D. D. Size-Dependent Tuning of Mn^{2+} d-Emission in Mn^{2+}-Doped CdS Nanocrystals: Bulk Vs Surface. *J. Phys. Chem. C* **2010**, *114*, 18323−18329.
(37) Yuan, X.; Zheng, J.; Zeng, R.; Jing, P.; Ji, W.; Zhao, J.; Yang, W.; Li, H. Thermal Stability of Mn^{2+} Ion Luminescence in Mn-Doped Core−Shell Quantum Dots. *Nanoscale* **2014**, *6*, 300−307.
(38) Yuan, X.; Ji, S.; De Siena, M. C.; Fei, L.; Zhao, Z.; Wang, Y.; Li, H.; Zhao, J.; Gamelin, D. R. Photoluminescence Temperature Dependence, Dynamics, and Quantum Efficiencies in Mn^{2+}-Doped $CsPbCl_3$ Perovskite Nanocrystals with Varied Dopant Concentration. *Chem. Mater.* **2017**, *29*, 8003−8011.
(39) Gahlot, K.; Pradeep, K. R.; Camellini, A.; Sirigu, G.; Cerullo, G.; Zavelani-Rossi, M.; Singh, A.; Waghmare, U. V.; Viswanatha, R. Transient Species Mediating Energy Transfer to Spin-Forbidden Mn d States in II−VI Semiconductor Quantum Dots. *ACS Energy Lett.* **2019**, *4*, 729−735.
(40) Pinchetti, V.; Anand, A.; Akkerman, Q. A.; Sciacca, D.; Lorenzon, M.; Meinardi, F.; Fanciulli, M.; Manna, L.; Brovelli, S. Trap-Mediated Two-Step Sensitization of Manganese Dopants in Perovskite Nanocrystals. *ACS Energy Lett.* **2019**, *4*, 85−93.
(41) Luo, B.; Guo, Y.; Li, X.; Xiao, Y.; Huang, X.; Zhang, J. Z. Efficient Trap-Mediated Mn^{2+} Dopant Emission in Two Dimensional Single-Layered Perovskite $(CH_3CH_2NH_3)_2PbBr_4$. *J. Phys. Chem. C* **2019**, *123*, 14239−14245.
(42) Sun, Q.; Wang, S.; Zhao, C.; Leng, J.; Tian, W.; Jin, S. Excitation-Dependent Emission Color Tuning from an Individual Mn-Doped Perovskite Microcrystal. *J. Am. Chem. Soc.* **2019**, *141*, 20089−20096.
(43) Justice Babu, K.; Kaur, G.; Shukla, A.; Kaur, A.; Goswami, T.; Ghorai, N.; Ghosh, H. N. Concurrent Energy- and Electron-Transfer Dynamics in Photoexcited Mn-Doped $CsPbBr_3$ Perovskite Nanoplatelet Architecture. *J. Phys. Chem. Lett.* **2021**, *12*, 302−309.
(44) Ricciarelli, D.; Meggiolaro, D.; Belanzoni, P.; Alothman, A. A.; Mosconi, E.; De Angelis, F. Energy Vs Charge Transfer in Manganese-Doped Lead Halide Perovskites. *ACS Energy Lett.* **2021**, *6*, 1869−1878.
(45) Pradhan, N.; Sarma, D. D. Advances in Light-Emitting Doped Semiconductor Nanocrystals. *J. Phys. Chem. Lett.* **2011**, *2*, 2818−2826.

https://doi.org/10.1021/acs.jpcc.2c06911
J. Phys. Chem. C 2022, 126, 21109−21116